Capillarity

Vol. 16, No. 2, p. 51-60, 2025

Original article

Developing and characterizing magnetic nanocomposites for effective metal ion removal in wastewater treatment

Yingtao Sun, Zhenhua Wei, Di Bian, Jianfeng Zhou*

School of Mechanical and Power Engineering, Nanjing Tech University, Nanjing 211816, P. R. China

Keywords:
Adsorption technology
magnetic nanocomposites
Fe_3O_4 nanoparticles
wastewater treatment
environmental remediation

Cited as:
Sun, Y., Wei, Z., Bian, D., Zhou, J. Developing and characterizing magnetic nanocomposites for effective metal ion removal in wastewater treatment. Capillarity, 2025, 16(2): 51-60.
https://doi.org/10.46690/capi.2025.08.03

Abstract:
This research explores the synthesis and application of magnetic nanocomposites as effective adsorbents for the removal of metal ions from wastewater. Using a chemical co-precipitation method, Fe_3O_4 nanoparticles were modified with branched polyethyleneimine and stover activated carbon, yielding Fe_3O_4/Branched-Polyethyleneimine and Fe_3O_4/Spherical-Activated-Carbon adsorbents. These materials were thoroughly characterized to confirm their functional groups and optimized surface structure for heavy metal uptake. Thanks to their paramagnetic properties, the adsorbents are easily recovered and readily recycled. Adsorption efficiency was systematically evaluated by varying contact time, Cu^{2+} concentration, and adsorbent dosage. Isotherm and kinetic models were applied to elucidate the adsorption mechanisms, with Fe_3O_4/Branched-Polyethyleneimine best described by the pseudo-second order kinetic model and the Sips isotherm. This study not only provides empirical evidence of the adsorbents' efficacy but also lays a conceptual foundation for their practical implementation in industrial wastewater treatment applications, paving the way for future advancements in adsorbent technology.

1. Introduction

Copper contamination represents a significant global environmental challenge owing to the widespread presence of copper and its compounds. Over the past decades, extensive efforts have been made to develop economical and environmentally friendly methods to mitigate copper contamination (Wang et al., 2025). The World Health Organization has identified even minimal concentrations of Cu^{2+} in water as a hindrance to natural self-purification processes, deeming water with levels exceeding 0.001 mg/L unsafe for consumption. The detrimental effects of copper pollution extend beyond human health, manifesting in acute poisoning of aquatic fauna and discoloration of oysters in coastal and harbor regions. Furthermore, elevated copper levels are linked to serious health issues-such as lung cancer and gastrointestinal infections-representing a substantial public health concern in high-exposure populations. This situation highlights the urgent need for the efficient removal of Cu^{2+} from effluents before they are discharged into aquatic ecosystems (Tian et al., 2020).

Adsorbent technology, recognized for its cost-effectiveness and high removal capacity, has become a preferred method for extracting heavy metal ions from aqueous solutions and soils (Shao et al., 2023). This approach circumvents the limitations commonly associated with conventional processes-such as filtration, electrochemical treatment, and ion exchange-which are often costly and complex. Recently, a range of innovative adsorbents has been developed for the removal of Cu^{2+}. For instance, Wang et al. (2021) employed cement solidified materials, while Yang et al. (2021a) utilized functionalized gel beads. Additionally, natural and modified sorbents-including pine bark (Nguyen et al., 2025), chitosan-based fibers (Niu et

Yandy Scientific Press

*Corresponding author.
E-mail address: Yingtao.sun@connect.ust.hk (Y. Sun); weizhenhua157359@163.com (Z. Wei); bd@njtech.edu.cn (D. Bian); zhoujianfeng@njtech.edu.cn (J. Zhou).

Received May 28, 2025; revised June 19, 2025; accepted July 10, 2025; available online July 13, 2025.

Table 1. Experimental materials.

Experiment	Material	Manufacturer
Preparation of Fe_3O_4	Ferrous chloride	China, Shanghai Runjie Chemical Products Co., Ltd
	Ferric chloride	China, Shanghai Runjie Chemical Products Co., Ltd
	Ammonia water	China, Nanjing WANQING Chemical Glassware & Instrument Co., Ltd
Preparation of Fe_3O_4/SAC	Stover activated carbon	China, Shanghai Titan Scientific Co., Ltd
	Ultra pure water	China, Nanjing zebra Experimental Equipment Co., Ltd
Preparation of Fe_3O_4/BPEI	Ethyl [3-propyl] carbodiimide hydrochloride	China, Nanjing shengjianquan chemical Glass Instrument Co., Ltd
	Sodium hydroxide standard solution	China, Nanjing WANQING chemical Glassware & Instrument Co., Ltd
	Branched polyethyleneimide	China, Beijing Inno Chem Science & Technology Co., Ltd

al., 2019), pomelo peel (Begum et al., 2013), and bentonite (Alraae et al., 2025)-have demonstrated high adsorption efficiencies. Despite these advantages, such materials can pose drawbacks, including potential secondary pollution, operational complexity, and elevated costs.

This study examines the synthesis and application of magnetic materials, which have undergone significant advancements and found diverse uses in microwave technology (Kubrakova and Pryazhnikov, 2021), adsorption processes (Kelarijani et al., 2020; Litvinov, 2020; Zheng et al., 2021; Sun et al., 2023), oncology (Li et al., 2020), photocatalysis (BioLegend, 2020; Liu et al., 2023), and sealing technologies (Yang et al., 2021b, 2022; Mitamura et al., 2022; Sun et al., 2024). In wastewater treatment, magnetic materials have demonstrated considerable utility. Schiff base-functionalized Fe_3O_4 effectively adsorbs Hg^{2+} and Ag^{+} (Miao et al., 2020), while Inbaraj et al. (2021) employed a magnetic activated carbon nanocomposite to remove polycyclic aromatic hydrocarbons. Ren et al. (2021) used MgO functionalized magnetic activated carbon to extract Malachite Green, and Sugumar et al. (2021) reported strong complexation between Branched Polyethyleneimine (BPEI) and Cu^{2+}.

Recognizing the sensitivity of magnetic adsorbents to their aqueous environment and the critical role of surface chemistry, we synthesized three functional magnetic adsorbents-bare Fe_3O_4, Fe_3O_4/Spherical-Activated-Carbon (SAC), and Fe_3O_4/BPEI-to engineer a simple yet effective system for Cu^{2+} removal suitable for industrial implementation. Surface and magnetic properties were characterized by Vibrating Sample Magnetometry and Transmission Electron Microscopy (TEM). We systematically investigated the influence of operational parameters-such as contact time, initial Cu^{2+} concentration, and adsorbent dosage-on removal efficiency. To elucidate the underlying mechanisms, we applied a suite of equilibrium isotherm models (Redlich-Peterson, Toth, Sips, Hill) and kinetic models (Weber-Morris intraparticle diffusion, Elovich, pseudo-first-order, and pseudo-second-order), which have proven particularly appropriate for copper adsorption (Jiang et al., 2023).

2. Experiments

2.1 Materials

Three adsorbents were prepared in this study. The materials used are listed in Table 1.

2.2 Synthesis of adsorbents

2.2.1 Fe_3O_4 magnetic nanoparticles (MPs)

Magnetic Particles (MPs) were synthesized via chemical co precipitation of ferrous chloride ($FeCl_2$) and ferric chloride ($FeCl_3$) according to the following five step procedure:

1) Ferric chloride solution: Dissolve 50 grams of $FeCl_3$ in 500 mL of deionized water under mechanical stirring at 600 rpm.
2) Ferrous chloride solution: Separately dissolve 16 grams of $FeCl_2$ in 100 mL of deionized water with magnetic stirring for 20 minute under a nitrogen atmosphere.
3) Mixing: Combine the $FeCl_2$ solution with the $FeCl_3$ solution under continuous stirring for 25 minute.
4) Precipitation: Collect the resulting precipitate by vacuum filtration.
5) Drying: Dry the wet precipitate under vacuum at 100 °C for 24 hour.

The overall reaction for Fe_3O_4 nanoparticle formation can be represented as:

$$2Fe^{3+} + Fe^{2+} + 8NH_3 \cdot H_2O \rightarrow Fe_3O_4 + 8NH_4{}^{+} + 4H_2O \quad (1)$$

2.2.2 SAC-modified Fe_3O_4 (Fe_3O_4/SAC)

The adsorbent preparations were carried out as follows:

1) Carbon preparation: 10.0 grams of stover activated carbon were placed in a 100 mL stoppered cylinder.
2) Mixing with MPs: 10.0 grams of MPs were added, and the mixture was homogenized thoroughly.
3) Magnetic separation: The wet composite was collected by applying an external magnetic field.
4) Drying: The composite was dried under vacuum at 100 °C for 24 h.

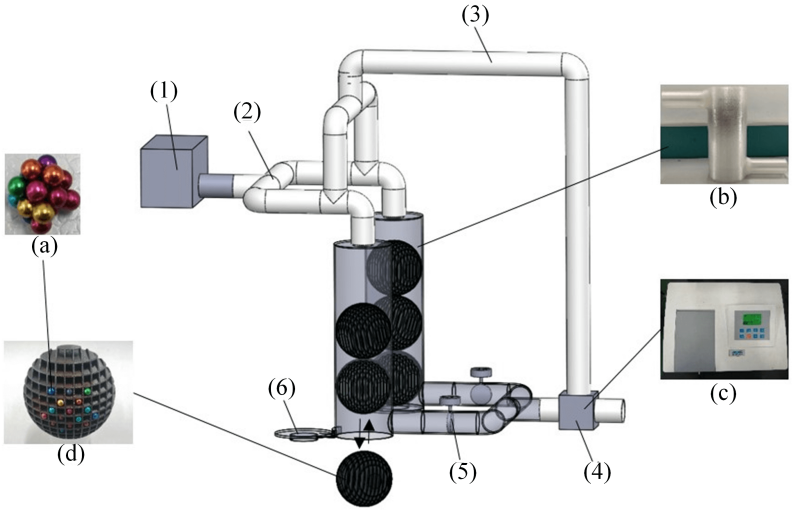

Fig. 1. Treatment system for wastewater containing metal ions. (a) Magnetic structure, (b) wastewater treatment structure, (c) spectrophotometer, and (d) porous pellet. 1: Metal ions-containing wastewater tank, 2: Diverter tube, 3: Recirculation pipe, 4: Monitoring station with compression and shunt ability, 5: Valve, 6: Quick-access cover.

2.2.3 BPEI-modified Fe_3O_4 (Fe_3O_4/BPEI)

This adsorbent preparation is shown as follows:

1) MPs preparation: 10.0 grams of MPs were transferred into a beaker containing 200 mL of deionized water.
2) pH adjustment: The solution pH was adjusted to 6.0 using hydrochloric acid, after which 1 ethyl 3 (3-dimethylaminopropyl) carbodiimide hydrochloride and N-hydroxysuccinimide were added.
3) BPEI addition: A 200 mL solution of BPEI was introduced, and the mixture was stirred under vacuum for 24 h.
4) Magnetic separation: The functionalized MPs were recovered magnetically.
5) Drying: The product was dried under vacuum at 100 °C for 24 h.

2.3 Experiment methods

2.3.1 Cu^{2+} adsorption experiment

Process variables investigated included temperature (25-50 °C), contact time (5-100 min), adsorbent dosage (0.5-5.0 g/L), and initial Cu^{2+} concentration (10-150 mg/L). The adsorption rate (A) of Cu^{2+} was calculated using Eq. (2), and each experiment was performed in quintuplicate to minimize error. Thermodynamic measurements were conducted at pH 6 and temperatures from 10 to 80 °C. Data on the effects of contact time and Cu^{2+} concentration were used to evaluate adsorption kinetics and isotherms, respectively. The equilibrium uptake (q_e) was calculated as:

$$A = \frac{c_1 - c_2}{c_1} \times 100\% \tag{2}$$

$$q_e = \frac{(c_0 - c_e) \times V}{n} \tag{3}$$

where A is the adsorption rate, and c_1 as well as c_2 are the solution's instantaneous concentration. The c_0 and c_e reflect the initial and equilibrium content of Cu^{2+} ions. V denotes the volume of the used liquid, and n represents the amount of adsorbent in Eq. (3).

Kinetic data were fitted to pseudo-first order, pseudo-second order, Elovich, and Weber-Morris intraparticle diffusion models. Thermodynamic parameters were derived using the Van't Hoff equation. Equilibrium data were modeled with the Redlich-Peterson, Toth, Sips, and Hill isotherms, which have been shown to describe Cu^{2+} adsorption effectively Hussain et al. (2023).

2.3.2 Desorption and reusability assessment

To assess desorption efficiency and adsorbent reusability, the following procedure was employed. After Cu^{2+} adsorption, the spent adsorbents were recovered by filtration and magnetic separation. They were then immersed in 0.05 M HCl and stirred magnetically for 24 h to desorb Cu^{2+}. Subsequently, the adsorbents were separated magnetically, rinsed with deionized water until the washings reached neutral pH, and dried at 100 °C for 1 h. The regenerated adsorbents were then reused in subsequent Cu^{2+} removal cycles.

3. Wastewater treatment system

3.1 Treatment process

The treatment apparatus is illustrated in Fig. 1. Copper-containing wastewater enters the system and is split into two parallel streams, each passing through an adsorbent-packed section. After adsorption, effluent from both streams flows through an online Cu^{2+} monitoring station. Streams that satisfy the discharge criteria are either sent on for further processing or released directly, whereas those that do not meet the standards are routed back via a recirculation loop for additional treatment. In Fig. 1(b), a porous pellet holder is shown at the midpoint of the piping; Fig. 1(d) depicts that these pellets accommodate small magnetic beads, which serve as the ads-

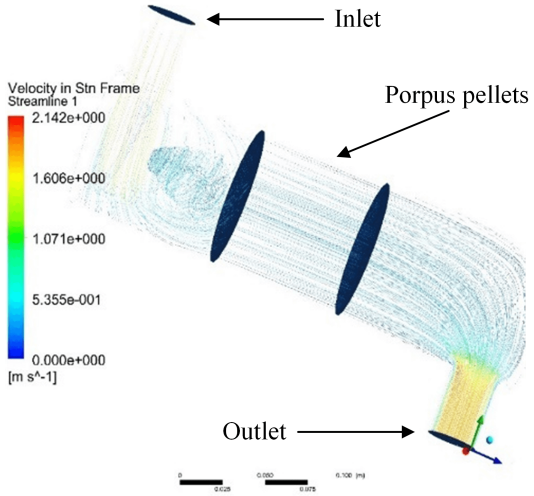

Fig. 2. Flow streamlines of fluid around porous pellets.

Table 2. Surface properties and characteristics of samples.

Sample	Fe_3O_4	Fe_3O_4/SAC	Fe_3O_4/BPEI
BET surface area (m^2/g)	69.697	77.375	67.472
Total pore volume (cm^3/g)	0.214	0.251	0.248
Average pore size (nm)	9.732	18.357	16.287

orbent phase. The bead diameter is chosen to match the pellet pore channels, as shown in Fig. 1(a), ensuring efficient retention under an applied magnetic field.

3.2 Validation by flow field

To verify the fluid flow within the pipeline after introducing porous media, ANSYS Fluent was employed for Computational Fluid Dynamics (CFD) simulations. The porous zone model in Fluent applies to both single-phase and multiphase flows and encompasses components such as packed beds, filter papers, perforated plates, flow distributors, and tube bundles. A one-dimensional simplification-often termed "porous jump"-enables the representation of thin porous films with predefined pressure drop or velocity characteristics. The porous jump formulation is implemented as a porous face treatment rather than a volumetric cell zone, enhancing numerical robustness and convergence.

Within the model, any region designated as "porous" is assigned empirically determined resistance coefficients (Oliveira et al., 2023; Zheng et al., 2025). Mechanically, the porous media model introduces an additional momentum sink term into the Navier-Stokes equations. This source term comprises two components-viscous loss and inertial loss-expressed as:

$$S_i = -\left(\sum_{j=1}^{3} D_{ij}\mu v_j + \sum_{j=1}^{3} C_{ij}\frac{1}{2}\rho|\boldsymbol{v}|v_j\right) \quad (4)$$

where S_i is the momentum sink in the i-th (x, y, or z direction) momentum equation, ρ is the density, μ is the dynamic viscosity of the fluid, and D_{ij} and C_{ij} are given matrices. Besides, v_j is the velocity component of the three coordinate directions of x, y, and z, and $|\boldsymbol{v}|$ is the magnitude of the velocity vector.

For simple, homogeneous porous media, the momentum sink term can be expressed in its most compact form as:

$$S_i = -\left(\frac{\mu}{\alpha}v_i + C_2\frac{1}{2}\rho|\boldsymbol{v}|v_i\right) \quad (5)$$

where α is the viscous resistance coefficient (related to $1/K$, with K being the permeability), and C_2 is the inertial resistance coefficient. Besides, v_i is the local velocity component.

As shown in Fig. 2, the central segment of the pipeline depicted in Fig. 1(b) was extracted for CFD analysis. A velocity-inlet boundary condition was imposed at the upstream end, while a pressure-outlet condition was prescribed at the downstream end. The midsection was modeled as a porous medium to represent the packed pellets. The computational domain, discretized into 132,672 grid cells, was verified for mesh independence.

Porosity was specified as 0.80, and ANSYS Fluent was used to simulate the fluid flow. Fig. 2 demonstrates that flow recirculation intensifies adjacent to the walls, leading to enhanced retardation effects. This behavior arises from the separation vortex generated when the fluid encounters the first porous pellet, which functions as a bluff body. At the outlet, the reduction in cross-sectional area produces a localized acceleration, enabling the fluid to transition smoothly into the downstream pipeline.

4. Results and discussion

4.1 Material characterization

4.1.1 Microstructural analysis

The microstructure of the magnetic nanocomposite adsorbents was elucidated by TEM (Figs. 3(a)-3(c)). Pristine Fe_3O_4 particles appear as nearly spherical nanocrystals with a range of diameters; their size and morphology can be tuned via synthesis temperature or surfactant choice. The high density of interstices between primary Fe_3O_4 grains suggests abundant accessible sites for Cu^{2+} binding. Upon incorporation of SAC or BPEI, the apparent particle diameter increases markedly, confirming successful composite formation. Fe_3O_4/SAC exhibits a rough surface with nanoscale pores-likely generated by the evolution of volatile byproducts (e.g., H_2O, CO, CO_2) during carbon activation (Oliveira et al., 2023)- whereas Fe_3O_4/BPEI particles display core-shell architectures, with Fe_3O_4 cores uniformly coated by polymer layers.

4.1.2 Surface area and porosity

Brunauer-Emmett-Teller (BET) analysis (Table 2; N_2 adsorption-desorption isotherms and pore-size distributions in Fig. S1) further differentiates these materials. All three samples possess sizeable specific surface areas, underscoring the role of porosity in enhancing adsorption capacity (Morán et

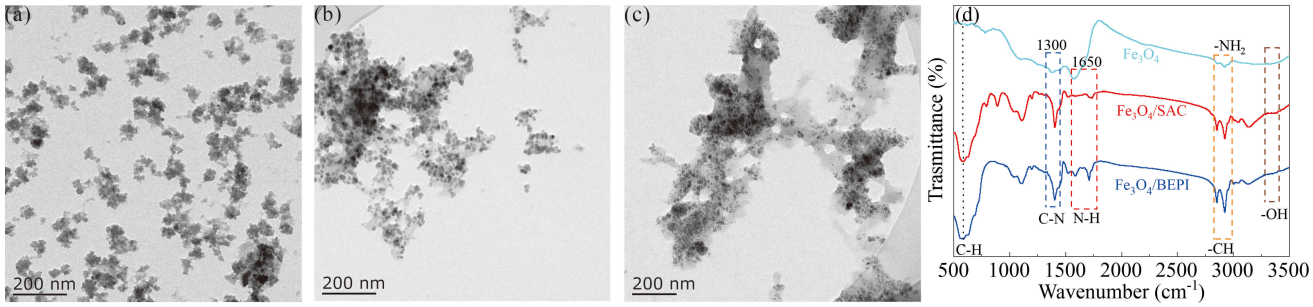

Fig. 3. TEM results: (a) Fe_3O_4, (b) Fe_3O_4/SAC, (c) Fe_3O_4/BPEI, and (d) FTIR result. Comparative spectra of Fe_3O_4, Fe_3O_4/SAC, and Fe_3O_4/BPEI.

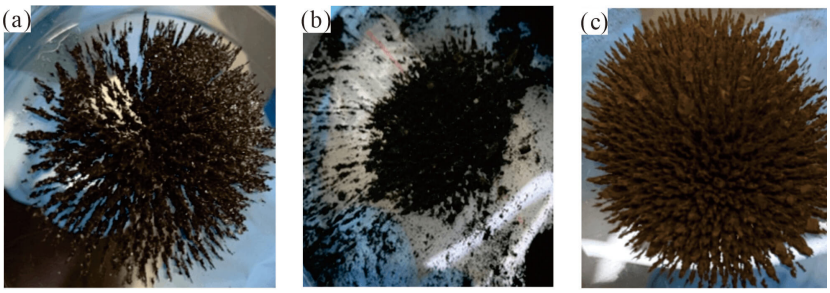

Fig. 4. Samples response under applied magnetic field. (a) Fe_3O_4, (b) Fe_3O_4/SAC, and (c) Fe_3O_4/BPEI.

al., 2023; Xiao et al., 2023). Composite materials (Fe_3O_4/SAC and Fe_3O_4/BPEI) exhibit larger average pore diameters than bare Fe_3O_4, consistent with TEM observations and indicating a predominantly mesoporous network (Yu et al., 2023).

4.1.3 Chemical composition

FTIR spectra (Fig. 3(d)) reveal distinct functional-group profiles. Fe_3O_4/BPEI displays strong absorptions at $2,875-2,970$ (C-H), 1,551-1,630 (N-H), and 1,250-1,376 cm^{-1} (C-N), reflecting abundant amine functionalities known to chelate Cu^{2+} via HSAB interactions and protonation-mediated complexation (Duan et al., 2023; Tański et al., 2023; Rijk et al., 2023). In contrast, Fe_3O_4 and Fe_3O_4/SAC show only $-$OH and Fe-O stretching bands at $\sim 3,345-3,465$ cm^{-1} and $\sim 1,100$ cm^{-1}, with Fe_3O_4/SAC additionally exhibiting O-C-O vibrations that can contribute to pH-dependent electrostatic adsorption (Poggere et al., 2023; Li et al., 2023).

4.1.4 Magnetic properties

A common concern with surface modification is the potential loss of superparamagnetic (Kergoat et al., 2023). This issue may impede the recycling process and potentially introduce more contaminants. However, all three materials retained rapid magnetic responsiveness (Fig. 4), aggregating swiftly under an external field. Vibrating Sample Magnetometry measurements (Fig. 5) confirm their superparamagnetic nature: the hysteresis loops show negligible coercivity, and saturation magnetizations of Fe_3O_4, Fe_3O_4/SAC, and Fe_3O_4/BPEI were 86.3, 39.1, and 35.1 emu/g, respectively. These results demonstrate that despite composite formation, the adsorbents maintain both robust magnetic separability and high adsorption potential (Eom et al., 2023).

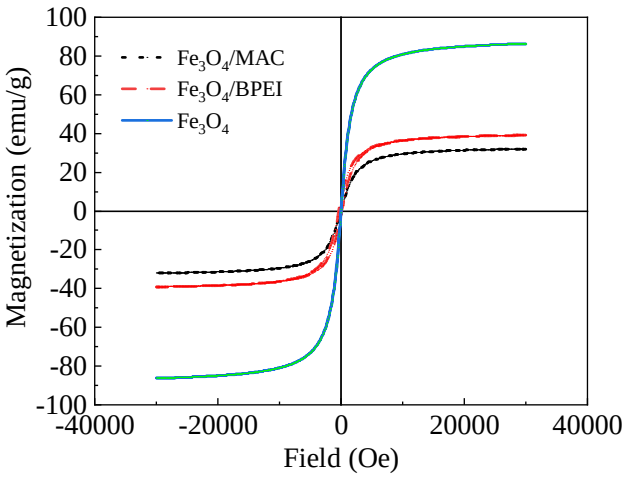

Fig. 5. VSM magnetization curves.

4.2 Adsorption kinetics

Nonlinear regression was used to determine the constants and variables of the dynamic models; the resulting parameter values are summarized in Table 3. Kinetic analysis of Cu^{2+} removal revealed that the adsorption by Fe_3O_4 and Fe_3O_4/SAC conforms best to the Pseudo-First Order model, whereas Fe_3O_4/BPEI follows the Pseudo-Second Order (PSO) model. This distinction implies that Fe_3O_4/BPEI adsorption involves both chemisorption and physisorption mechanisms, while Fe_3O_4 and Fe_3O_4/SAC predominantly undergo physical adsorption. High coefficients of determination ($R^2 \approx 1$) confirm the excellent fit and substantial adsorption capacities of all three materials (Järvinen et al., 2023).

From Table 3, the Elovich model parameters α and β for

Table 3. Constants and kinetic variables determined for the Cu^{2+} adsorption.

Model	Parameters	Fe_3O_4	Fe_3O_4/SAC	Fe_3O_4/BPEI
Pseudo-first order	q_e	2.0190	6.2349	6.0002
	K_1	0.0573	0.0438	0.0689
	R^2	0.9864	0.9733	0.9852
	RMSE	0.0136	0.1030	0.0764
	Adj R^2	0.9858	0.9722	0.9832
Pseudo-second order	q_e	2.3026	6.7892	6.5783
	K_2	0.0302	0.0062	0.0136
	R^2	0.9733	0.9659	0.9897
	RMSE	0.0379	0.2997	0.0612
	Adj R^2	0.9713	0.9633	0.9872
	α (mg/g·min)	0.5135	0.7963	2.4239
	β (g/mg)	0.3727	0.7036	0.8725
	R^2	0.9431	0.9326	0.9831
	RMSE	0.1038	0.1893	0.5964
	Adj R^2	0.9421	0.9298	0.9818
Intraparticle diffusion	$K_{i,1}$ (mg/g·min$^{1/2}$)	0.2969	0.8257	0.7769
	C_1 (mg/g)	-0.0254	-0.2478	0.6024
	R^2	0.9865	0.9733	0.9827
	$K_{i,2}$ (mg/g·min$^{1/2}$)	0.1016	0.1203	0.1706
	C_2 (mg/g)	1.1124	5.0236	4.3684
	R^2	0.9238	0.6783	0.9833
	$K_{i,3}$ (mg/g·min$^{1/2}$)	0.0133	0.4039	-0.0204
	C_3 (mg/g)	1.9370	6.2037	6.1036
	R^2	0.3567	0.0774	0.6038

Notes: In the Elovich equation, where α is the initial adsorption rate constant (mg/g·min), β is the desorption constant related to surface coverage (g/mg).

Table 4. Thermodynamic parameters derived from the Van't-Hoff equation.

Samples	T (K)	ΔG (kJ/mol)
Fe_3O_4 $\Delta H = -5.98$ KJ/mol $\Delta S = -14.83$ KJ/mol	298	-1.41
	303	-1.58
	308	-1.46
	313	-1.36
	318	-1.28
	323	-1.22
	328	-1.08
	333	-0.98
Fe_3O_4/SAC $\Delta H = -9.11$ KJ/mol $\Delta S = -9.48$ KJ/mol	298	-6.23
	303	-6.27
	308	-6.19
	313	-6.21
	318	-6.14
	323	-5.91
	328	-6.03
	333	-5.95
Fe_3O_4/BPEI $\Delta H = 10.17$ KJ/mol $\Delta S = 55.16$ KJ/mol	298	-6.20
	303	-6.65
	308	-6.73
	313	-7.11
	318	-7.43
	323	-7.64
	328	-7.94
	333	-8.15

Fe_3O_4, Fe_3O_4/SAC, and Fe_3O_4/BPEI are 0.51 and 0.37, 0.80 and 0.70, and 2.42 and 0.87, respectively. The notably higher α and β values for Fe_3O_4/BPEI indicate its superior adsorption rate and capacity within a given contact time (Abdel-Azim et al., 2023).

4.3 Thermodynamic analysis

Thermodynamic parameters were evaluated using the Van't Hoff relationships (Eqs. (6) and (7)). Fig. 6(b) presents the linearized Van't Hoff plot, and the derived values of ΔH, ΔS, and ΔG are listed in Table 4:

$$\ln K_f = \frac{\Delta S}{R} - \frac{\Delta H}{RT} \tag{6}$$

$$\Delta G = -RT \ln K_f \tag{7}$$

where ΔH is standard enthalpy, ΔS is standard entropy, ΔG is Gibbs free energy, K_f is the adsorption distribution coefficient, R (= 8.314 J·mol^{-1}K^{-1}) is the gas constant, and T is the absolute temperature.

Temperature critically influences both mass transfer and the adsorption kinetics of Cu^{2+} (Holubčík et al., 2022). Fig. 6(a) shows that, for Fe_3O_4 and Fe_3O_4/SAC, removal efficiencies decrease from 85.26% to 52.33% and from 30.36% to 15.80%, respectively, as the temperature rises from 298 to 333 K, indicating exothermic adsorption. An increase in temperature enhances the diffusion rate of Cu^{2+} ions-thereby increasing their mobility in solution-while simultaneously weakening the adsorbent-ion interactions. Thermodynamically, this behavior corresponds to a less favorable Gibbs free energy for adsorption at higher temperatures, since the enthalpic term becomes more influential and physical bonding forces diminish, leading to greater desorption of Cu^{2+} back into the aqueous phase (Han et al., 2022).

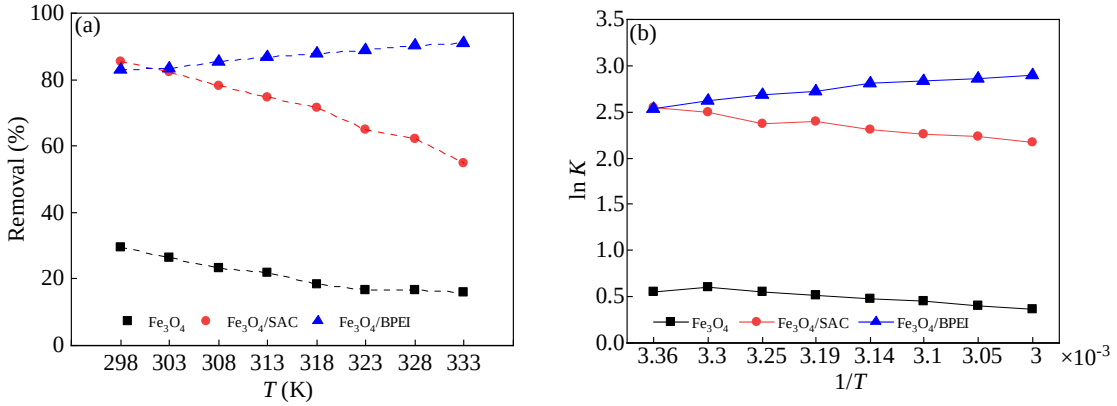

Fig. 6. Thermodynamic analysis. (a) Temperature dependence of removal and (b) linearized Van't-Hoff relation.

Table 5. Isotherm model parameters.

Model	Parameters	Fe_3O_4	Fe_3O_4/SAC	Fe_3O_4/BPEI
Redlich-Peterson (R-P)	K	8.2239	16.2573	19.3989
	a	4.1369	1.7932	0.9635
	b	0.9364	0.9387	0.9796
	RSS	0.0262	3.8964	5.6721
	R^2	0.9587	0.9866	0.9873
	Adj R^2	0.9499	0.9859	0.9798
Toth	q_m	7.9337	21.4369	23.3694
	b	0.2893	1.6735	1.8325
	n	0.2423	1.1338	0.9987
	RSS	0.0363	4.3682	5.9368
	R^2	0.9737 0.9937	0.9878	
	Adj R^2	0.9694	0.9878	0.9781
Sips	K	3.6891	19.3654	17.2358
	α_s	0.8204	0.8316	0.7323
	β	0.3318	1.2359	0.9952
	RSS	0.0274	4.1568	5.7327
	R^2	0.9678	0.9936	0.9858
	Adj R^2	0.9534	0.9866	0.9773
Sips	q_m	4.3680	25.7261	33.1571
	K	1.4560	1.3862	1.9721
	n	0.3507	1.1037	0.4504
	RSS	0.0242	3.9603	1.8484
	R^2	0.9604	0.9876	0.9945
	Adj R^2	0.9598	0.9804	0.9902

Notes: R-P: $q_e = K_R C_e/(1+a_R C_e^g)$; Toth: $q_e = K_T C_e/(a_T + C_e)^{1/t}$; Sips: $q_e = K_S C_e^\beta S/(1+a_S C_e^\beta S)$; Hill: $q_e = q_{SH} C_e^{nH}/(K_D + C_e^{nH})$.

Conversely, Fe_3O_4/BPEI exhibits increased adsorption efficiency with temperature (298 to 333 K), consistent with an endothermic mechanism. From the Van't Hoff analysis (Table 4), ΔG values range from -0.9 to -8.2 kJ/mol, confirming that Cu^{2+} uptake is spontaneous under all conditions studied. The positive enthalpy change ($\Delta H^\circ = +10.17$ kJ/mol) for Fe_3O_4/BPEI further substantiates an endothermic, chemisorptive process, whereas the Fe_3O_4 and Fe_3O_4/SAC systems display exothermic, physisorption-dominated behavior. Moreover, the positive entropy change (ΔS) for Fe_3O_4/BPEI indicates increased randomness at the solid-liquid interface during adsorption (Palani et al., 2022; Zhu et al., 2023).

4.4 Adsorption isotherm

A recent review identified the Redlich-Peterson, Toth, Sips, and Hill isotherm models as particularly well-suited for Cu^{2+} adsorption (Alomari et al., 2023). Table 5 summarizes the fitted parameters and nonlinear-regression results for these models applied to Fe_3O_4, Fe_3O_4/SAC, and Fe_3O_4/BPEI. In all cases, high coefficients of determination (R^2) confirm excellent agreement between the experimental data and model predictions.

In the Sips isotherm, the amount adsorbed at equilibrium (q_e) is related to the equilibrium concentration (C_e) by the equation in Table 5, where K_s is the Sips affinity constant and β is the heterogeneity exponent. When $\beta = 1$, the Sips model reduces to the classical Langmuir isotherm (homogeneous monolayer adsorption). At low C_e, it approximates the Freundlich isotherm, thereby capturing heterogeneous, multisite adsorption behavior.

For Fe_3O_4/BPEI, the Redlich-Peterson model achieves an R^2 of 0.988, indicating a hybrid adsorption mechanism that deviates from ideal monolayer behavior (Kim et al., 2022). Likewise, the Sips fit for Fe_3O_4/BPEI yields $\beta = 0.995$ and $K_s = 0.732$, values close to unity that imply adsorption predominantly via discrete functional sites on the composite surface.

Finally, comparison of the maximum adsorption capacities (q_{max}) shows that our magnetic composites perform favorably relative to other Cu^{2+} adsorbents reported in the literature.

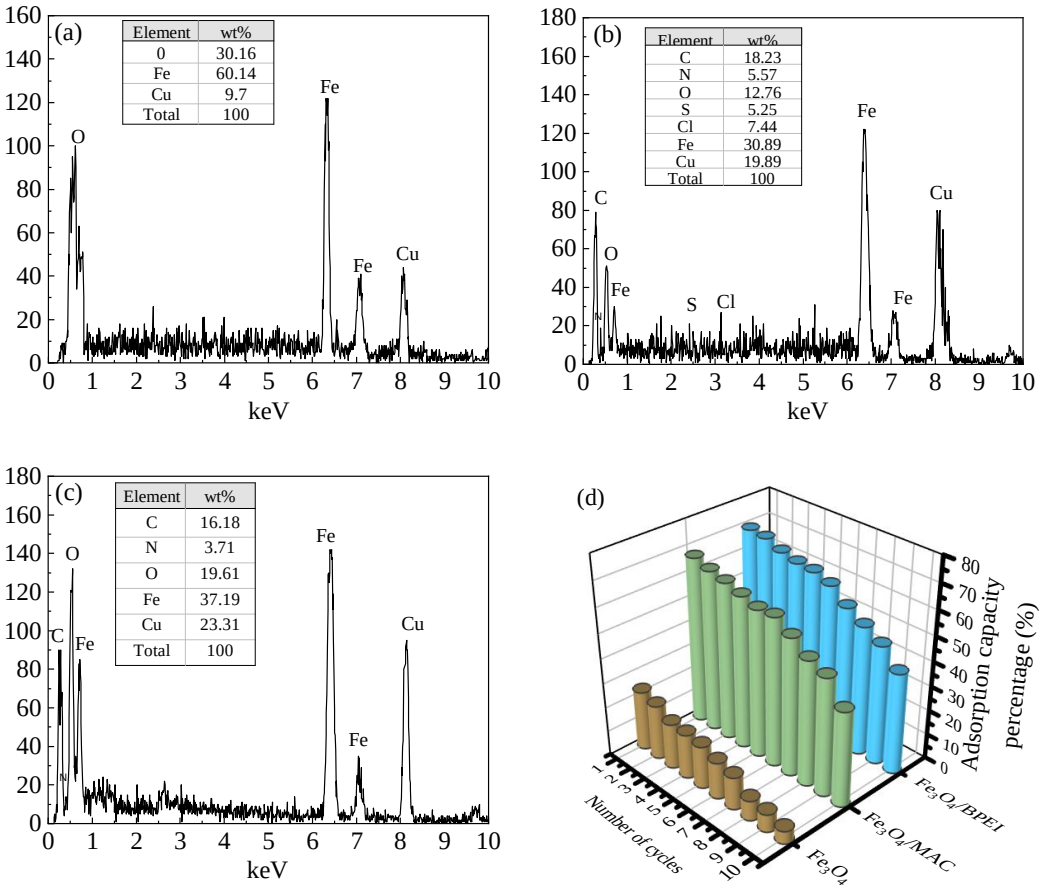

Fig. 7. EDS results: (a) Fe_3O_4, (b) Fe_3O_4/SAC, (c) Fe_3O_4/BPEI, and (d) influence of the sorption/desorption cycles on the equilibrium sorption capacities.

Table 6. Comparison of the maximum adsorption capacity.

Adsorbent	q_{max} (mg/g)	Reference
BC600	43.75	Wang et al. (2022)
BC400	30.70	Wang et al. (2022)
RSBC700	52.5	Mei et al. (2020)
FSM400	11.45	Meng et al. (2014)
CSM400	12.82	Meng et al. (2014)
FSM700	8.93	Meng et al. (2014)
CSM700	9.76	Meng et al. (2014)
Fe_3O_4	4.37	Present study
Fe_3O_4/SAC	25.73	Present study
Fe_3O_4/BPEI	33.16	Present study

This enhanced performance likely arises from synergistic interactions between Fe_3O_4, SAC, and BPEI components, which collectively increase the density and accessibility of active adsorption sites.

4.5 Reusability performance

Energy-Dispersive X-ray Spectroscopy (EDS) analyses (Figs. 7(a)-7(c)) confirmed that Cu^{2+} removal is attributable to the adsorbents themselves, rather than to variations in temperature or pH. After adsorption, the Fe content remained essentially unchanged, whereas the signals for K and Ca diminished, and a clear Cu signal emerged. Moreover, Fe_3O_4/BPEI exhibited the highest relative Cu uptake compared to Fe_3O_4 and Fe_3O_4/SAC.

Economic considerations and sorbent reusability were evaluated through ten desorption-adsorption cycles. Regeneration was performed by treating the spent adsorbents with 0.05 M HCl for 24 h. Fig. 7(d) shows that the minimum adsorption efficiencies after ten cycles were 7.58% for Fe_3O_4, 48.31% for Fe_3O_4/SAC, and 57.89% for Fe_3O_4/BPEI. The superior retention of performance by the structurally dependent composites (Fe_3O_4 and Fe_3O_4/SAC) versus Fe_3O_4/BPEI likely reflects the chemical degradation of surface functional groups during acid treatment, whereas the core-shell and porous structures remain intact.

Finally, Table 6 compares the maximum adsorption capacities (q_{max}) of our adsorbents with those of various reported materials. The capacities reported here are moderate relative to the literature, reflecting the dual physicochemical adsorption

mechanisms inherent to our magnetic composites.

5. Conclusions

In this study, Fe_3O_4/BPEI and Fe_3O_4/SAC magnetic nanocomposites demonstrated efficient Cu^{2+} removal from aqueous solutions via spontaneous, endothermic chemisorption ($\Delta G = -0.9$ to -8.2 kJ/mol; $\Delta H = +10.17$ kJ/mol). Equilibrium data were best described by heterogeneous isotherm models (Redlich-Peterson, Toth, Sips, Hill), with the amine-rich surface of Fe_3O_4/BPEI exhibiting the highest adsorption capacity. Both composites retained superparamagnetic behavior, enabling rapid magnetic separation and facile regeneration. These attributes position the materials as practical, scalable adsorbents for heavy metal remediation, warranting further validation in pilot-scale studies and exploration of their applicability to additional contaminants.

Acknowledgements

The authors thank the fund for its financial support, which allowed the experiment to be carried out smoothly. This work was supported by the National Natural Science Foundation of China (No. 52175171) and the Postgraduate Research & Practice Innovation Program of Jiangsu Province (No. KYCX25_1746).

Supplementary file

https://doi.org/10.46690/capi.2025.08.03

Conflict of interest

The authors declare no competing interest.

References

Abdel-Azim, W. E., Elserougi, A. A., Hossam-Eldin, A. A. A modular switched-capacitor voltage multiplier-based multi-module high-voltage pulse generator for electrostatic precipitators applications. Alexandria Engineering Journal, 2023, 65: 503-520.

Alomari, M., Rashid, M. U., Chadalavada, P., et al. Comparison between metabolic-associated fatty liver disease and nonalcoholic fatty liver disease: From nomenclature to clinical outcomes. World Journal of Hepatology, 2023, 15(4): 477.

Alraae, A., Moussadik, A., Benzaouak, A., et al. Cu nanoparticles-decorated beidellite: Synthesis, characterization, and catalytic reduction of wastewater pollutants. Colloids and Surfaces A: Physicochemical and Engineering Aspects, 2025, 718: 136885.

Begum, N., Noorliyana, A., Bari, M. F., et al. Kinetic and thermodynamic studies on adsorption of copper ions onto pomelo peel (Citrus grandis). Advanced Materials Research, 2013, 795: 674-678.

BioLegend, Inc. Stable nanomagnetic particle dispersions. U.S., 20160320376, 2020.

Duan, M., Li, Z., Yan, R., et al. Mechanism for combined application of biochar and bacillus cereus to reduce antibiotic resistance genes in copper contaminated soil and lettuce. Science of The Total Environment, 2023, 884: 163422.

Eom, Y. S., Kang, D. H., Choi, D. H. Feasibility of applying an electrostatic precipitator integrated with a naturally ventilated double-skin façade in residential buildings. Journal of Building Engineering, 2023, 68: 106065.

Han, Y., Xiao, L., Chen, H. Chemical agglomeration to enhance blast furnace dust capture efficiency in wet electrostatic precipitators. Coatings, 2022, 12(12): 1937.

Holubčík, M., Drga, J., Čajová Kantová, N., et al. Optimization of discharging electrodes of a multi-chamber electrostatic precipitator for small heat sources. Atmosphere, 2022, 14(1): 63.

Hussain, M., Hussaini, S. S., Shariq, M., et al. Enhancing Cu^{2+} ion removal: an innovative approach utilizing modified frankincense gum combined with multiwalled carbon tubes and iron oxide nanoparticles as adsorbent. Molecules, 2023, 28(11): 4494.

Inbaraj, B. S., Sridhar, K., Chen, B. H. Removal of polycyclic aromatic hydrocarbons from water by magnetic activated carbon nanocomposite from green tea waste. Journal of Hazardous Materials, 2021, 415: 125701.

Järvinen, A., Lehtoranta, K., Aakko-Saksa, P., et al. Performance of a wet electrostatic precipitator in marine applications. Journal of Marine Science and Engineering, 2023, 11(2): 393.

Jiang, L., Li, N., Li, X., et al. Phytoremediation of copper-contaminated soils by drip or sprinkling irrigation coupled with intercropping. Environmental Science and Pollution Research, 2023, 30(33): 81303-81313.

Kelarijani, A. F., Zanjani, N. G., Pirzaman, A. K. Ultrasonic assisted transesterification of rapeseed oil to biodiesel using nano magnetic catalysts. Waste and Biomass Valorization, 2020, 11(6): 2613-2621.

Kergoat, L., Dabrin, A., Masson, M., et al. Clogging modulates the copper effects on microbial communities of streambed sediments. Ecotoxicology, 2023, 32(3): 321-335.

Kim, Y. S., Lee, Y., Kim, Y. J., et al. Improvement of an in-duct two-stage electrostatic precipitator via diffusion charging. Toxics, 2022, 10(11): 686.

Kubrakova, I. V., Pryazhnikov, D. V. Microwave-assisted synthesis of nanosized magnetic sorbents. Journal of Analytical Chemistry, 2021, 76: 15-25.

Li, T., Yang, C., Wei, Z., et al. Recent advances of magnetic nanomaterials in the field of oncology. OncoTargets and Therapy, 2020, 13: 4825-4832.

Litvinov, D. Nanomagnetism and nanomagnetic materials. IEEE Nanotechnology Magazine, 2020, 14(1): 5.

Liu, S., Hubao, A., Tang, S., et al. Molecular insights into structural and dynamic properties of water molecules in calcium silicate hydrate nanopores: The roles of pore size and temperature. Capillarity, 2023, 8(2): 23-33.

Li, Y., Mu, D., Wu, H., et al. Derivation of copper water quality criteria in Bohai Bay for the protection of local

aquatic life and the ecological risk assessment. Marine Pollution Bulletin, 2023, 190: 114863.

Mei, Y., Li, B., Fan, S. Biochar from rice straw for Cu^{2+} removal from aqueous solutions: Mechanism and contribution made by acid-soluble minerals. Water, Air, & Soil Pollution, 2020, 231(8): 420.

Meng, J., Feng, X., Dai, Z., et al. Adsorption characteristics of Cu (II) from aqueous solution onto biochar derived from swine manure. Environmental Science and Pollution Research, 2014, 21: 7035-7046.

Miao, J., Liu, A., Wu, L., et al. Magnetic ferroferric oxide and polydopamine molecularly imprinted polymer nanocomposites based electrochemical impedance sensor for the selective separation and sensitive determination of dichlorodiphenyltrichloroethane (DDT). Analytica Chimica Acta, 2020, 1095: 82-92.

Mitamura, Y., Nishimura, I., Yano, T. Thermal analysis of a miniature magnetic fluid seal installed in an implantable rotary pump. Journal of Magnetism and Magnetic Materials, 2022, 548: 168977.

Morán, J., Li, L., Ouyang, H., et al. Characterization of the bidimensional size and charge distribution of sub-and supermicrometer particles in an electrostatic precipitator. Powder Technology, 2023, 425: 118578.

Nguyen, A. H., Gunawardhana, T., Siddiqui, S. I., et al. An enzymatically modified adsorbent derived from an agro-residue mitigates the environmental risks of toxic antibiotic mixtures. Environmental Research, 2025, 270: 121038.

Niu, Y., Ying, D., Jia, J. Continuous adsorption of copper ions by chitosan-based fiber in adsorption bed. Journal of Environmental Engineering, 2019, 145(8): 04019041.

Oliveira, A. F., Machado, R. B., Ferreira, A. M., et al. Copper-contaminated substrate biosorption by Penicillium sp. isolated from kefir grains. Microorganisms, 2023, 11(6): 1439.

Palani, S., Mathivanan, A., Kumar, A. Low cost and compact electrostatic precipitator model controlled by smoke detector. IOP Conference Series: Earth and Environmental Science. IOP Publishing, 2022, 1100(1): 012029.

Poggere, G., Gasparin, A., Barbosa, J. Z., et al. Soil contamination by copper: Sources, ecological risks, and mitigation strategies in Brazil. Journal of Trace Elements and Minerals, 2023, 4: 100059.

Ren, Z., Yang, Z., Zhao, Z., et al. MgO functionalized magnetic activated carbon material for efficient removal of malachite green from aqueous solutions. Nano, 2021, 16(5): 2150054.

Rijk, I., Berkelund, L., Ekblad, A., et al. Effects of copper contamination on N cycling microbial guilds and plant performance in two contrasting grassland soils. Soil Biology and Biochemistry, 2023, 180: 109015.

Shao, W., Yang, J., Wang, H., et al. Recent research progress on imbibition system of nanoparticle-surfactant dispersions. Capillarity, 2023, 8(2): 34-44.

Sugumar, K., Vignesh, G., Arunachalam, S. A comparative study on interactions of ternary copper (ii) complexes and their analogues anchored polymer (bpei) with serum albumins. Chemistry Select, 2021, 6(22): 5387-5398.

Sun, Y., Chen, J, Wei, Z., et al. Copper ion removal from aqueous media using banana peel biochar/Fe_3O_4/branched polyethyleneimine. Colloids and Surfaces A: Physicochemical and Engineering Aspects, 2023, 658: 130736.

Sun, Y., Wei, Z., Zhou, J., et al. Modification of magnetorheological fluid and its compatibility with metal skeleton: Insights from multi-body dissipative particle dynamics simulations and experimental study. Physics of Fluids, 2024, 36(3): 032020.

Tański, M., Reza, A., Przytuła, D., et al. Electrostatic precipitator with surface dielectric barrier discharge ionizer. Journal of Cleaner Production, 2023, 404: 136990.

Tian, F., Zhou, J., Shao, C., et al. Effective recovery of oil slick using the prepared high hydrophobic and oleophilic Fe_3O_4 magnetorheological fluid. Colloids and Surfaces A: Physicochemical and Engineering Aspects, 2020, 591: 124531.

Wang, X., Ma, S., Wang, X., et al. The mechanism of Cu^{2+} sorption by rice straw biochar and its sorption-desorption capacity to Cu^{2+} in soil. Bulletin of Environmental Contamination and Toxicology, 2022, 109(3): 562-570.

Wang, Y., Li, Z., Yang, N., et al. Kinetics of copper ion leaching from cement-solidified body of blast furnace slag adsorbing copper ion. Materials Science Forum, 2021, 1035: 1036-1042.

Wang, Z., Li, S., Xu, Z., et al. Advances and challenges in foam stability: Applications, mechanisms, and future directions. Capillarity, 2025, 15(3): 58-73.

Xiao, L., Zhai, X., Han, Y., et al. Experimental study on humidification coagulation and removal of fine particles using an electrostatic precipitator. Polymers, 2023, 15(9): 2065.

Yang, L., Zhang, X., Yang, J., et al. A rhodamine-based chemosensor and functionalized gel ball for detecting and adsorbing copper ions. Tetrahedron, 2021a, 80: 131893.

Yang, X., Guan, Y., Huang, Y. Numerical and experimental study of the embedded magnetic fluid seal with a small gap. Physica Scripta, 2021b, 96(12): 125023.

Yang, X., Song, Y., Sun, P., et al. Design and experimental study on divergent magnetic fluid seal with large clearance and dual magnetic sources. Advances in Materials Science and Engineering, 2022, 2022(1): 4637689.

Yu, Z., Liu, J., Shen, R., et al. An efficient thumbtack-cylinder type wet electrostatic precipitator for moxa smoke aerosol control. Powder Technology, 2023, 424: 118562.

Zheng, L., Jiang, J., Xiao, W., et al. A NMR investigation of spontaneous and forced imbibition of shale under different flow and confinement conditions. Capillarity, 2025, 14(2): 53-62.

Zheng, X., Zhang, X., Hu, Q., et al. Adsorption and photocatalytic activity of nano-magnetic materials Fe_3O_4@C@TiO_2-AgBr-Ag for rhodamine B. Current Nanoscience, 2021, 17(3): 484-493.

Zhu, Y., Tao, S., Liu, J., et al. Experimental research of capture enhancement mechanism of submicron particles by designing two-stage electrostatic precipitators with various ratios of charger and collector units. Chemical Engineering Research and Design, 2023, 189: 52-63.